ELSEVIER

Theoretical and Applied Fracture Mechanics 38 (2002) 15–36

theoretical and applied fracture mechanics

www.elsevier.com/locate/tafmec

Damage analysis of tetragonal perovskite structure ceramics implicated by asymptotic field solutions and boundary conditions

G.C. Sih [a,b,*], Z.F. Song [c]

[a] *Institute of Mechanics, Chinese Academy of Sciences, Beijing 100080, China*
[b] *Department of Mechanical Engineering and Mechanics, Lehigh University, Bethlehem, PA 18015, USA*
[c] *Department of Engineering Mechanics, Xi'an Jiaotong University, 710049 Xi'an Shaanxi, China*

Abstract

Cracking of ceramics with tetragonal perovskite grain structure is known to appear at different sites and scale level. The multiscale character of damage depends on the combined effects of electromechanical coupling, prevailing physical parameters and boundary conditions. These detail features are exhibited by application of the energy density criterion with judicious use of the mode I asymptotic and full field solution in the range of $r/a = 10^{-4}$ to 10^{-2} where r and a are, respectively, the distance to the crack tip and half crack length. Very close to the stationary crack tip, bifurcation is predicted resembling the dislocation emission behavior invoked in the molecular dynamics model. At the macroscopic scale, crack growth is predicted to occur straight ahead with two yield zones to the sides. A multiscale feature of crack tip damage is provided for the first time. Numerical values of the relative distances and bifurcation angles are reported for the PZT-4 ceramic subjected to different electric field to applied stress ratio and boundary conditions that consist of the specification of electric field/mechanical stress, electric displacement/mechanical strain, and mixed conditions. To be emphasized is that the multiscale character of damage in piezoceramics does not appear in general. It occurs only for specific combinations of the external and internal field parameters, elastic/piezoelectric/dielectric constants and specified boundary conditions.

1. Introduction

When stress is applied to a ferroelectric material such as barium titanate $BaTiO_3$, a change in polarization may occur. This results in a small voltage across the specimen accompanied by a small deformation. The effect is known as "piezoelectricity". The same behavior prevails when a ferroelectric material is subjected to an external electric field such that alignment of the dipole moments of several domain would occur and polarization is said to have taken place. The conversion of mechanical strain into electricity is utilized in devices known as transducers; they may include strain gages, microphones, sona detectors, phonograph pickups, etc. The inverse mechanism

* Corresponding author. Address: School of Advanced Science and Technology, Xi'an Jiaotong University, Box No. 1175, 710049 Xi'an Shaanxi, China. Fax: +86-29-266-8028.
E-mail address: gcs@xjtu.edu.cn (G.C. Sih).

0167-8442/02/$ - see front matter © 2002 Published by Elsevier Science Ltd.
PII: S0167-8442(02)00078-2

where an electric field could change the dimensions of a ferroelectric material is called "electrostriction". It has equally wide applications.

Ferroceramics $BaTiO_3$, $PbZrTiO_6$, etc. and the alike, however, can crack prematurely under service conditions. A particular concern over the years has been the crack growth behavior in these materials that are affected by orientations of poling with reference to the applied electric field and/or mechanical stress. Experiments [1–3] have consistently showed that such effects can be significant. Up to now, attempts made to explain many of the observed experimental phenomena have not been completely successful. Problems associated with cracking of piezoceramics are multifaceted, particularly when the influence of mechanical imperfections is interwoven with other parameters. Among the outstanding areas related to cracking of piezoelectric materials are:

- *Non-linearity:* Multiscale character of damage caused by electrical–mechanical disturbances may involve energy dissipation at the different scale levels ahead of the crack. The electron structure of the piezoelectric material is affected by the elastic/piezoelectric/dielectric constants.

  Status quo: Non-linear Dugdale models assuming mechanical and electrical yielding [4] have been used to explain the crack growth behavior in [1–3]. Quantitative assessments of yielding along a line ahead of the crack are given by using the superposition of linear piezoelectric solutions. Other non-linear models have also been proposed [5–10]. They are concerned with microstructure changes caused by domain switching.
- *Boundary conditions:* Stress/electric field or strain/electric displacement field boundary conditions could alter the transfer of mechanical and electrical energy to the crack tip region in ways that are not always apparent.

  Status quo: Stress intensity and electric displacement field factors, energy release rates and path independent integrals have been derived using different boundary conditions [11,12]. No conclusive explanations have been offered for the difference in solutions. Strain/electric displacement field conditions have not been analyzed previously. Moreover, it was not obvious why the crack tip energy release rates would decrease to zero and become negative when the applied electric field is increase monotonically.
- *Fracture criteria:* Those failure criteria that are inherently based on taking the limit to approach the crack tip may contain restrictions that are not apparent at first sight. Asymptotic field solution may leave out certain aspects of the multiscale behavior.

  Status quo: Up to now, the energy release rate concept has been used exclusively to examine the fracture behavior of ferroelectric materials [11–15]. The conclusions, however, are not consistent; they tend to vary with application. Only recently that the energy density criterion has been applied [16–23] to offer a different approach for modeling the multiscale crack initiation problem.
- *Asymptotic approximation:* The general notion is that the asymptotic field solution would coincide with the full field solution in the limit as the crack tip is approached. Since the limiting process used in continuum mechanics makes no reference to any specific distances, it could be problematic when quantifying size scale that may vary from 10^{-8} to 10^{-2} cm. Inexactness of the asymptotic solution does not always decrease with distance to the crack. The deviation could be non-monotonic. That is the error could reach a maximum at a certain finite distance near the crack. This distance can vary from problem to problem depending on the geometry, loading and material.

  Status quo: For an elastic, isotropic and homogeneous medium, it has been known that for $r/a \leqslant 0.1$, the asymptotic crack solution would coincide with the full field solution. This result, however, may not hold for non-homogeneous and anisotropic materials and/or more complex boundary conditions. Discrepancies between the asymptotic and full field solution can differ from 10% to 90% in piezoelasticity; it is dictated by the nature of electromechanical coupling and boundary conditions.
- *Microstructure transformation:* The occurrence or absence of microstructure transformation in piezoceramics is by no means obvious. Even

when the remote external loadings may not reach yield and/or coercive force level, the state of affairs at the crack tip could be severely elevated to cause domain switching. Each specific situation should be evaluated rather than taken for granted. Moreover, microstructure transformation is inherently a non-equilibrium process [24,25] where the system inhomogeneity alters with time. There exists no local states that could represent the system, as a while.

Status quo: Polarization and depolarization of ferroelectric materials in connection with domain switching have been quantified in [7–10] for tetragonal perovskite type of structure using continuum mechanics. An energy density criterion was adopted to determine the thresholds of polarization switching. It is not clear that the critical energy density states referred to the crystal lattice could also apply to grains at the mesoscale. Depending on the temperature, polarization other than tetragonal such as the rhombohedral type could also take place.

In what follows, attempts are made to identify the potential variable that could affect the multiscale cracking behavior in piezoelectric materials. The PZT-4 ceramic will be used to provide numerical results for illustration. Special emphases are given to the ways with which asymptotic and full field solution could affect the outcome regardless of the fracture criterion. Moreover, the influence of boundary conditions should not be underestimated; they could alter the qualitative features of cracking in ceramics. It is felt that the implications of linear piezoelasticity should be understood in more depth prior to invoking nonlinearity that could in itself introduce additional uncertainties.

2. Plane strain crack problem in piezoelasticity

The constitutive relations for piezoelasticity show that the stresses σ_{ij} are linear functions of the strain ε_{ij} and electric field components E_i. The electric displacements D_i are also linear in the strains electric field components. That is

$$\sigma_{ij} = C_{ijkl}\gamma_{kl} - e_{kij}E_k, \qquad D_i = e_{ikl}\gamma_{kl} + \varepsilon_{ik}E_k \tag{1}$$

in which C_{ijkl}, e_{ijk} and ε_{ij} are, respectively, the elastic, piezoelectric and dielectric constants. This, however, does not imply that the electromechanical effects could be separated because σ_{ij} and γ_{ij} depend implicitly on E_i and/or D_i and vice versa. Their interdependence has been discussed in [19,20].

2.1. Poling along x_3-axis

The governing equations for piezoelasticity can be simplified if the axis of material symmetry coincides with those for the crack geometry. For plane deformation, let x_3 be along the poling direction and x_1 be directed along the crack plane as shown in Fig. 1. For the case of plane extension, expressions in Eq. (1) can be simplified as

$$\begin{bmatrix}\sigma_{11}\\ \sigma_{33}\\ \sigma_{31}\\ D_1\\ D_3\end{bmatrix} = \begin{bmatrix}c_{11} & c_{13} & 0 & 0 & e_{31}\\ c_{13} & c_{33} & 0 & 0 & e_{33}\\ 0 & 0 & c_{44} & e_{15} & 0\\ 0 & 0 & e_{15} & -\varepsilon_{11} & 0\\ e_{31} & e_{33} & 0 & 0 & -\varepsilon_{33}\end{bmatrix}\begin{bmatrix}\gamma_{11}\\ \gamma_{33}\\ \gamma_{31}\\ -E_1\\ -E_3\end{bmatrix} \tag{2}$$

For the PZT-4 ceramics under plane strain, the physical constants in Eq. (2) can be found in Table 1. The inverse of Eq. (2) become

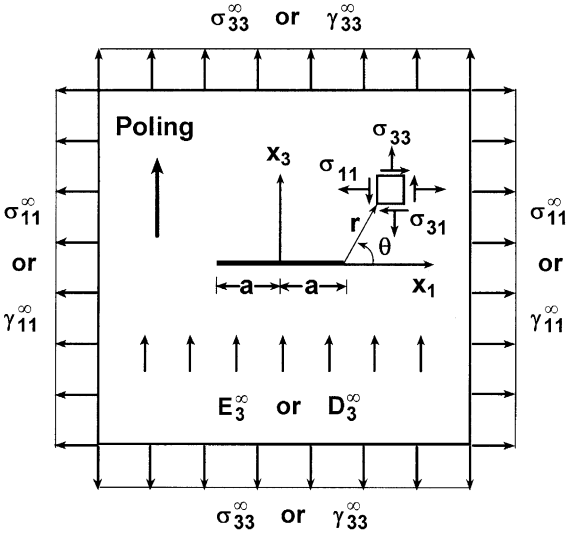

Fig. 1. Cracked piezoelectric medium under in-plane applied mechanical and electrical load.

Table 1
Material constants for PZT-4

Elastic constants $\times 10^{10}$ (N/m^2)				Piezoelectric constants (C/m^2)			Dielectric permittivities $\times 10^{-9}$ (C/V m)	
c_{11}	c_{13}	c_{33}	c_{44}	e_{31}	e_{33}	e_{15}	ε_{11}	ε_{33}
13.9	7.43	11.3	2.56	−6.98	13.84	13.44	6.00	5.47

$$\begin{bmatrix} \gamma_{11} \\ \gamma_{33} \\ \gamma_{31} \\ -E_1 \\ -E_3 \end{bmatrix} = \begin{bmatrix} a_{11} & a_{13} & 0 & 0 & b_{31} \\ a_{13} & a_{33} & 0 & 0 & b_{33} \\ 0 & 0 & a_{44} & b_{15} & 0 \\ 0 & 0 & b_{15} & -d_{11} & 0 \\ b_{31} & b_{33} & 0 & 0 & -d_{33} \end{bmatrix} \begin{bmatrix} \sigma_{11} \\ \sigma_{33} \\ \sigma_{31} \\ D_1 \\ D_3 \end{bmatrix} \tag{3}$$

The corresponding constants a_{11}, $a_{13}, \ldots$, etc. in Eq. (3) can be determined directly from those in Table 1.

2.2. Local elevation of energy density

The positive definiteness character of the energy density function $\mathrm{d}W/\mathrm{d}V$ is fundamental to the formulation of theories in mechanics and physics. In the theory of linear piezoelasticity, $\mathrm{d}W/\mathrm{d}V$ acquires the form

$$\mathrm{d}W/\mathrm{d}V = \frac{1}{2}\sigma_{ij}\gamma_{ij} + \frac{1}{2}D_iE_i \tag{4}$$

In the limit $r \to 0$ (Fig. 1), the electromechanical energy stored in a unit volume of material intensifies in accordance with the relation

$$\mathrm{d}W/\mathrm{d}V = \frac{S}{r} \quad \text{for } r \to 0 \tag{5}$$

Referring to Fig. 2, S represents the area $r(\mathrm{d}W/\mathrm{d}V)$ which is independent of the angle θ defined in Fig. 1. A small but finite distance $r_o \ll r$ is excluded from the analysis for otherwise the energy density would become unbounded at the crack tip. Such a requirement is in fact necessitated mathematically for the existence of the asymptotic expansion given in Eq. (5).

For the problem at hand, it has been shown in [19,20] that S can be expressed in terms of three intensity factors. That is

$$S = B_{11}K_{\mathrm{I}}^2 + B_{22}K_{\mathrm{II}}^2 + B_{44}K_{\mathrm{D}}^2 + 2B_{12}K_{\mathrm{I}}K_{\mathrm{II}} + 2B_{14}K_{\mathrm{I}}K_{\mathrm{D}} + 2B_{24}K_{\mathrm{II}}K_{\mathrm{E}} \tag{6}$$

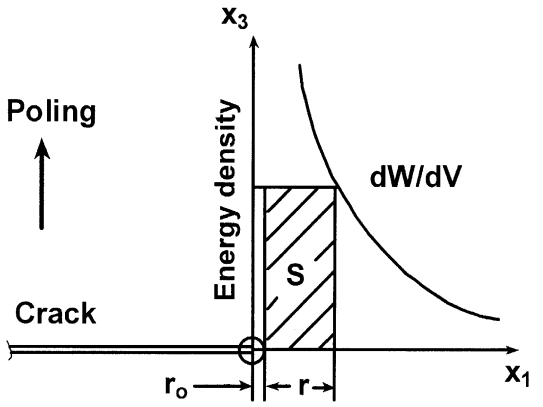

Fig. 2. Energy density decay near crack tip.

in which

$$K_{\mathrm{I}} = \sigma_{33}^{\infty}\sqrt{\pi a}, \qquad K_{\mathrm{II}} = \sigma_{31}^{\infty}\sqrt{\pi a}, \qquad K_{\mathrm{E}} = E_3^{\infty}\sqrt{\pi a} \tag{7}$$

The quantities B_{ij} in Eq. (6) depend on the material constants in Table 1 and they vary with the angle θ. When D_3^{∞} is applied, K_{E} would be replaced by K_{D} and B_{ij} by A_{ij} in Eq. (6). The details can be found in [19,20].

The four different choices of specifying σ_{33}^{∞} or γ_{33}^{∞} and E_3^{∞} or D_3^{∞} with or without σ_{11}^{∞} or γ_{11}^{∞} will be considered. These combinations referred to as boundary conditions could affect the fracture initiation behavior in different ways. The outcome is case specific.

3. Boundary conditions and energy density factors

For mode I crack extension, symmetry across the x_1-axis requires that both σ_{31}^{∞} and K_{II} in Eq. (7) would vanish. Each of the four pairs $(\sigma_{33}^{\infty}, E_3^{\infty})$, $(\gamma_{33}^{\infty}, D_3^{\infty})$, $(\sigma_{33}^{\infty}, D_3^{\infty})$, and $(\gamma_{33}^{\infty}, E_3^{\infty})$ can be specified independently at a given time while the others would be treated as dependent quantities. They will be referred to as Problems I–IV.

3.1. Problem I—($p_\sigma = E_3^\infty/\sigma_{33}^\infty$)

For $K_{II} = 0$, Eq. (6) reduces to

$$S = K_I^2[B_{11} + B_{44}p_\sigma^2 + 2B_{14}p_\sigma] \tag{8}$$

Once σ_{33}^∞ and E_3^∞ are specified, σ_{11}^∞ and D_3^∞ would be fixed according to

$$\sigma_{11}^\infty = k_\sigma\sigma_{33}^\infty, \qquad D_3^\infty = \frac{1}{d_{33}}[E_3^\infty + b_{31}\sigma_{11}^\infty + b_{33}\sigma_{33}^\infty] \tag{9}$$

Note that k_σ is a scalar that determines the biaxiality of the normal stresses at infinity while the material constants b_{31}, b_{33}, and d_{33} can be found from those in Table 1 for PZT-4.

3.2. Problem II—($q_\gamma = D_3^\infty/\gamma_{33}^\infty$)

It is also possible to specify D_3^∞ and γ_{33}^∞ such that S could become

$$S = K_\gamma^2(C_{11} + 2C_{14}q_\gamma + C_{44}q_\gamma^2) \tag{10}$$

The strain and electric displacement intensity factors K_γ and K_D take the forms

$$K_\gamma = \gamma_{33}^\infty\sqrt{\pi a}, \qquad K_D = D_3^\infty\sqrt{\pi a} \tag{11}$$

Now that D_3^∞ and γ_{33}^∞ are chosen, σ_{11}^∞ and σ_{33}^∞ are no longer independent, i.e.,

$$\gamma_{11}^\infty = k_\gamma\gamma_{33}^\infty,$$
$$\sigma_{33}^\infty = \left[c_{13}k_\gamma + c_{33} + \frac{e_{33}(e_{31}k_\gamma + e_{33})}{\varepsilon_{33}}\right]\gamma_{33}^\infty - \frac{e_{33}}{\varepsilon_{33}}D_3^\infty \tag{12}$$

This would be equivalent to the second fundamental boundary value problem in elasticity.

The constants C_{11}, C_{14} and C_{44} in Eq. (10) are given by

$$C_{11} = A_{11}\left[c_{13}k_\gamma + c_{33} + \frac{e_{33}(e_{31}k_\gamma + e_{33})}{\varepsilon_{33}}\right]^2$$
$$C_{14} = \left(A_{14} - A_{11}\frac{e_{33}}{\varepsilon_{33}}\right)\left[c_{13}k_\gamma + c_{33} + \frac{e_{33}(e_{31}k_\gamma + e_{33})}{\varepsilon_{33}}\right]$$
$$C_{44} = A_{11}\frac{e_{33}^2}{\varepsilon_{33}^2} + A_{44} - 2A_{14}\frac{e_{33}}{\varepsilon_{33}} \tag{13}$$

The quantities A_{ij} are related to B_{ij} in Eq. (8) as

$$\begin{aligned} B_{11} &= A_{11} + 2A_{14}(b_{33} + k_\sigma b_{31})/d_{33} \\ &\quad + A_{44}[(b_{33} + k_\sigma b_{31})/d_{33}]^2, \\ B_{14} &= A_{14}/d_{33} + A_{44}(b_{33} + k_\sigma b_{31})/d_{33}^2, \\ B_{44} &= A_{44}d_{33}^2. \end{aligned} \tag{14}$$

3.3. Problem III—($q_\sigma = D_3^\infty/\sigma_{33}^\infty$)

The mixed boundary value problems in piezoelasticity would involved specifying D_3^∞ and σ_{33}^∞ and E_3^∞ and γ_{33}^∞. For Problem III, there prevails

$$S = K_I^2[A_{11} + A_{44}q_\sigma^2 + 2A_{14}q_\sigma] \tag{15}$$

in which K_I has already been defined by the first of Eqs. (7). The remote strain γ_{33}^∞ and electric field E_3^∞ are no longer independent:

$$\gamma_{33}^\infty = a_{13}\sigma_{33}^\infty, \qquad E_3^\infty = d_{33}D_3^\infty - (b_{31}k_\sigma + b_{33})\sigma_{33}^\infty \tag{16}$$

3.4. Problem IV—($p_\gamma = E_3^\infty/\gamma_{33}^\infty$)

The final combination involves the specification of E_3^∞ and γ_{33}^∞ with S given by

$$S = K_\gamma^2[D_{11} + 2D_{14}p_\gamma + D_{44}p_\gamma^2] \tag{17}$$

in which K_γ can be found in Eq. (11) and D_{ij} are given by

$$\begin{aligned} D_{11} &= A_{11}(c_{13}k_\gamma + c_{33})^2 + A_{44}(e_{13}k_\gamma + e_{33})^2 \\ &\quad + 2A_{14}(c_{13}k_\gamma + c_{33})(e_{13}k_\gamma + e_{33}) \\ D_{44} &= A_{11}e_{33}^2 + A_{44}\varepsilon_{33}^2 - 2A_{14}e_{33}\varepsilon_{33} \\ D_{14} &= A_{44}(e_{13}k_\gamma + e_{33})\varepsilon_{33} - A_{11}(c_{13}k_\gamma + c_{33})e_{33} \\ &\quad + A_{14}[(c_{13}k_\gamma + c_{33})\varepsilon_{33} - (e_{13}k_\gamma + e_{33})e_{33}] \end{aligned} \tag{18}$$

The electric displacement D_3^∞ and stress σ_{33}^∞ are no longer independent since they are now

$$\begin{aligned} \sigma_{33}^\infty &= (k_\gamma c_{13} + c_{33})\gamma_{33}^\infty - e_{33}E_3^\infty, \\ D_3^\infty &= (k_\gamma e_{31} + e_{33})\gamma_{33}^\infty - \varepsilon_{33}E_3^\infty \end{aligned} \tag{19}$$

in which k_γ is defined by the first of Eqs. (12). This completes a brief description of Problem IV.

4. Asymptotic solution

At the damage sites, the material microstructure is known to be highly inhomogeneous and anisotropic, the details of which are not always critical if attention is focused at the macroscopic scale where the bulk properties could provide sufficient information. As the scale level of observation is reduced, however, the microscopic entities may no longer be negligible. Cracking of PZT ceramics tends to cover a wide range of size scale in contrast to isotropic and homogeneous materials where damage is highly localized. Whether the asymptotic solution would be adequate for describing the multiscale character of crack growth is a concern of this study.

4.1. Energy density criterion

The energy density fracture criterion [26,27] has been widely used for studying crack growth behavior in isotropic and elastoplastic materials. The practice is to analyze damage initiation sites at a fixed distance from the crack tip. This implies that the treatment is concerned with a single angular space variable for determining the stationary values of S. The procedure involves finding the relative minimum of S or $S_{\min}$ where dilatation would dominate. Such a location is assumed to correspond with damage initiation while the relative maximum of S or $S_{\max}$ would correspond to damage at a lower scale. An analogy would be elastic damage for $S_{\min}$ in contrast to plastic damage for $S_{\max}$. Mathematically, there could be many minima and maxima of $S_{\min}$ and $S_{\max}$. The maximum of $S_{\min}$ and maximum of $S_{\max}$ denoted as $(S_{\min}^{\max}, S_{\max}^{\max})$ would first reach the respective thresholds for cracking and yielding at the macroscopic scale. The same criterion holds for other scales except that different terminologies would be used. Microscopically speaking, the description could involve dislocations and submicroscopic defects that have not yet been completely understood.

To be emphasized is that the energy density fracture criterion remains valid regardless of the size and geometry of the imperfections that triggers damage initiation. They could be inhomogeneities involving dislocations, microdefects or macrocracks. The corresponding stresses and/or strains associated with the assumed type of defects are independent of the choice of failure criterion. The state of affairs near a dislocation would obviously differ from those for a line crack configuration. More specifically, the form of Eq. (5) for a micro- or macro-crack would not hold for a dislocation where $\mathrm{d}W/\mathrm{d}V$ would no longer be inversely proportional to the distance r. Unless otherwise stated, the asymptotic form of Eq. (5) is taken to be valid in this work.

4.2. Numerical values of S_{min}

Referring to the crack configuration in Fig. 1, the maximum of minimum S denoted by $S_{\min}^{\max}$ will be normalized to S_{o}. It will be written as $S^* = S_{\min}^{\max}/S_{\mathrm{o}}$ where S_{o} for Problems I–IV will be defined accordingly.

Problem I. For the PZT-4 material, the maximum of minimum S are found numerically. This gives the values of θ_{o} in B_{11}, B_{14}, and B_{44} at which S becomes $S_{\min}^{\max}$ for different $p_\sigma = E_3^\infty/\sigma_3^\infty$. The variations of S^* with p_σ are displayed in Fig. 3 by curves for different k_σ. All curves suffer a discontinuity. For $k_\sigma = 0$, no $S_{\min}$ occurred from $p_\sigma = -0.03$ to -0.024 V m/N. The normalization factor S_{o} represents S in Eq. (8) for $p_\sigma = k_\sigma = 0$ at

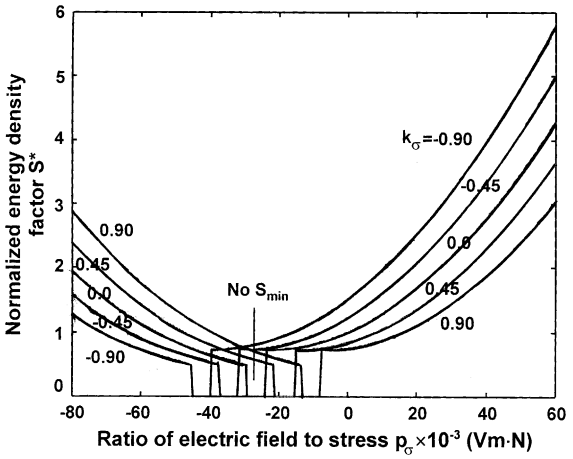

Fig. 3. Normalized energy density factor verus electric field to stress ratio for Problem I.

Table 2
Discontinuous intervals of p_σ for $S_{\min}$ as k_σ varies for Problem I

Biaxial stress factor $k_\sigma = \sigma_{11}^\infty/\sigma_{33}^\infty$				
−0.90	−0.45	0	0.45	0.90
[−0.045, −0.040]	[−0.037, −0.032]	[−0.029, −0.024]	[−0.021, −0.015]	[−0.013, −0.008]

$\theta_o = 0°$; it is numerically equal to $S_o = 4.837 \times 10^{-12}(\sigma_{33}^\infty)^2$ m/Pa. There is no apparent reason to explain for the broken segments of the curves in Fig. 3. Other intervals of p_σ within which no $S_{\min}$ were found for $k_\sigma \neq 0$ can be found in Table 2.

Aside from the peculiarities of the results in Table 2, bifurcation is predicted for certain combinations of p_σ and k_σ. These results can be found in Table 3 for increasing k_σ and decreasing p_σ. This is not expected because bifurcation is normally related to a moving crack with speed approaching the terminal velocity.

For most situations, Table 3 shows that crack initiation is predicted to occur along the line $\theta_o = 0°$ as expected for mode I crack extension.

Problem II. When D_3^∞ and γ_{33}^∞ are specified, Eq. (10) will be used to compute S while $S_o = 7.714 \times 10^{10}(\gamma_{33}^\infty)^2$ Pa m corresponds to S for $q_\gamma = k_\gamma = 0$ and $\theta_o = 0°$. Plotted in Fig. 4 are curves for $k_\gamma = 0$, ± 0.45 and ± 0.90 as the ratio q_γ is varied from −40 to 100 C/m^2. The trend for S^* is seen to decrease

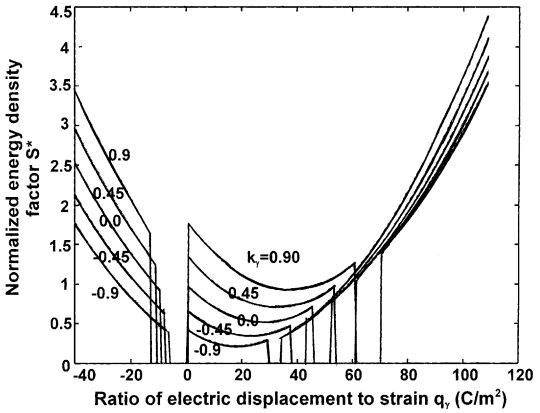

Fig. 4. Normalized energy density factor verus electric displacement to strain ratio for Problem II.

and then increase as q_γ is increased. Each of the five curves is discontinuous in the interval from −15 to 0 C/m^2. The corresponding intervals of q_γ for which $S_{\min}$ do not exist are given in Table 4. Reported in Table 5 are the predicted angles of crack growth initiation. The bifurcation angles $\pm\theta_o$ are seen to increase with increasing k_γ and q_γ

Table 3
Predicted S^* on crack initiation angles for Problem I

$p_\sigma \times 10^{-3}$ (V m/N)	Biaxial stress factor $k_\sigma = \sigma_{11}^\infty/\sigma_{33}^\infty$									
	−0.90		−0.45		0		0.45		0.90	
	S^*	θ_o (deg.)	S^*	θ_o (deg.)	S^*	θ_o (deg.)	S^*	θ_o (deg.)	S^*	θ_o (deg.)
−90	1.66	±73.3	2.05	±72.3	2.50	±71.8	3.01	±71.6	3.57	±71.6
−70	0.95	±80.2	1.19	±76.3	1.49	±74.1	1.85	±72.8	2.67	±72.1
−50	0.56	±112.6	0.69	±92.2	0.85	±83.0	1.06	±78.0	1.33	±75.0
−40	–	–	0.53	±123.9	0.65	±95.5	0.80	±84.8	1.0	±79.0
−30	0.77	0	0.73	0	0.50	±142.3	0.62	±99.8	0.76	±86.9
−25	0.83	0	0.75	0	–	–	0.55	±117.6	0.67	±93.8
−20	0.91	0	0.79	0	0.73	0	–	–	0.59	±105.3
−10	1.16	0	0.95	0	0.81	0	0.74	0	–	–
0	1.51	0	1.22	0	1.0	0	0.84	0	0.75	0
10	1.97	0	1.60	0	1.29	0	1.05	0	0.88	0
⋮	⋮	⋮	⋮	⋮	⋮	⋮	⋮	⋮	⋮	⋮
60	5.81	0	5.02	0	4.30	0	3.64	0	3.05	0

Table 4
Discontinuous intervals of q_γ for $S_{\min}$ as k_γ varies for Problem II

Biaxial strain factor $k_\gamma = \gamma_{11}^\infty/\gamma_{33}^\infty$				
−0.90	−0.45	0.0	0.45	0.90
[−6.0, 0]	[−7.5, 0]	[−9.0, 0.5]	[−10.5, 0.5]	[−12.5, 0.5]
[30.0, 40.0]	[38.0, 43.0]	[46.0, 52.0]	[54.0, 61.0]	[61.5, 70.0]

Table 5
Predicted S^* on crack initiation angles for Problem II

q_γ (C/m^2)	Biaxial strain factor $k_\gamma = \gamma_{11}^\infty/\gamma_{33}^\infty$									
	−0.90		−0.45		0.0		0.45		0.90	
	S^*	θ_o (deg.)	S^*	θ_o (deg.)	S^*	θ_o (deg.)	S^*	θ_o (deg.)	S^*	θ_o (deg.)
−50	2.40	±86.7	2.80	±89.4	3.25	±92.0	3.73	±94.6	4.25	±97.1
−40	1.78	±89.3	2.14	±92.5	2.54	±95.8	2.97	±98.8	3.44	±101.8
⋮	⋮	⋮	⋮	⋮	⋮	⋮	⋮	⋮	⋮	⋮
0	–	–	–	–	–	–	–	–	–	–
10	0.26	0	0.46	0	0.71	0	1.02	0	1.40	0
⋮	⋮	⋮	⋮	⋮	⋮	⋮	⋮	⋮	⋮	⋮
60	1.11	±72.4	1.05	±77.2	1.03	±92.8	–	–	1.25	0
70	1.59	±71.7	1.48	±73.3	1.42	±78.8	1.40	±93.5	–	–

stopping short at $q_\gamma = 0$ where no stationary values of S were found. This strange character will be further examined in relation to the approximate nature of Eq. (5). Note that branching is interrupted when q_γ becomes positive. The interruption occurs within an interval that tends to become larger as $D_3^\infty/\gamma_{33}^\infty$ or q_γ is increased. The solutions for $\theta_o = 0°$ at $k_\gamma = 0.90$ extended from $q_\gamma = 10$ to 60 C/m^2 in contrast to those for $k_\gamma = -0.90$ correspond to $q_\gamma = 10$ to 20 C/m^2. Trends of the data for $q_\gamma = -30$ to -10 C/m^2 and 20–50 C/m^2 in Table 5 are similar to those shown; they are not included to save space.

Problem III. Calculation of S^* for Problem III involves a knowledge of A_{ij} in Eq. (15) which are related to B_{ij} in Eq. (14). Again $S_o = 3.52 \times 10^8 (D_3^\infty)^2$ in S^* corresponds to $q_\sigma = 0$ and $\theta_o = 0°$. Fig. 5 for $k_\sigma = 0$ shows that S^* would decrease when q_σ increases until $q_\sigma = -5 \times 10^{-11}$ C/N; a discontinuity appears where $S_{\min}$ ceases to exist. Stationary values of S appear again for $q_\sigma > 0$ as shown in Table 6 and the curve in Fig. 5. Table 6 summarize the values of q_σ and S^* for which bifurcation occurs. They correspond to those for a single crack branch.

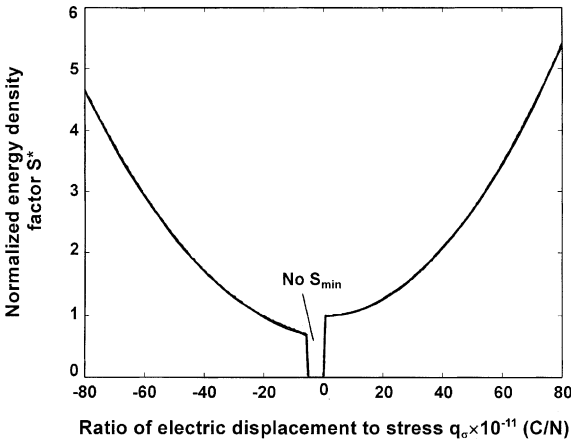

Fig. 5. Normalized energy density factor verus electric displacement to strain ratio for Problem II for $k_\sigma = 0$.

Problem IV. The curves in Fig. 6 for Problem IV have the same trend as those in Fig. 4 for Problem II where the biaxial strain factor k_γ is varied. For different k_γ, there exists two discontinuous intervals of p_γ within which $S_{\min}$ could not be found. A more detailed account of this peculiar feature can be seen from the numerical results in Table 7. In the majority of cases, the asymptotic

Table 6
Predicted crack initiation angles with $k_\sigma = 0$ for Problem III

$q_\sigma \times 10^{-11}$ (C/N)	−80	−60	−40	−20	−10	0	10	20	40	60	80
S^*	4.67	2.94	1.72	0.99	0.77	–	1.06	1.26	2.08	3.47	5.42
θ_o (deg.)	±71.6	±72.2	±75.7	±89.4	±113.2	–	0	0	0	0	0

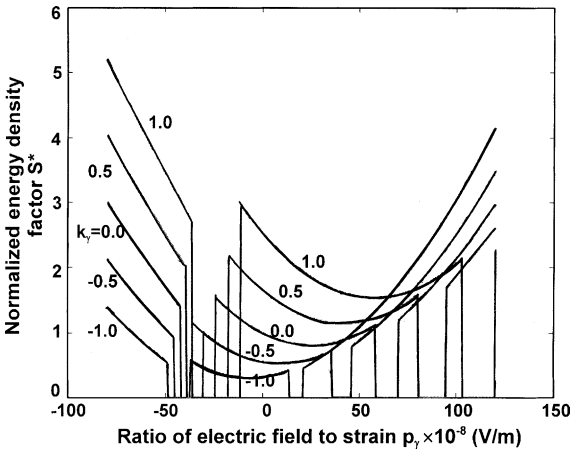

Fig. 6. Normalized energy density factor verus electric field to strain ratio for Problem IV.

solution predicts crack to initiate along the line of local symmetry, $\theta_o = 0°$. Those data in Table 8 that do not reveal any new trends have been deleted.

5. Full field solution

Even though the electrical and mechanical effects are coupled in piezoelasticity, the four types of boundary conditions referred to as Problems I–IV involved the specification of only three independent quantities (σ_{33}^∞, σ_{31}^∞, D_3^∞) for the asymptotic solutions discussed earlier. The other quantities such as $\sigma_{11}^\infty, \gamma_{11}^\infty, \ldots, D_1^\infty, E_1^\infty$, etc. are not independent. A description of the full field solution

Table 7
Predicted S^* on crack initiation angles for Problem IV

$p_\gamma \times 10^{-8}$ (V/m)	Biaxial strain factor $k_\gamma = \gamma_{11}^\infty/\gamma_{33}^\infty$									
	−1.0		−0.5		0		0.5		1.0	
	S^*	θ_o (deg.)	S^*	θ_o (deg.)	S^*	θ_o (deg.)	S^*	θ_o (deg.)	S^*	θ_o (deg.)
−90	1.77	±93.4	2.58	±96.0	3.53	±98.0	4.64	±99.7	5.90	±101.1
−70	1.10	±103.0	1.75	±105.1	2.55	±106.7	3.50	±107.9	4.61	±108.8
−50	0.57	±143.0	1.06	±134.4	1.71	±130.0	2.51	±127.0	3.46	±125.2
⋮	⋮	⋮	⋮	⋮	⋮	⋮	⋮	⋮	⋮	⋮
0	0.32	0	0.55	0	1.0	0	1.67	0	2.56	0
10	0.39	0	0.52	0	0.88	0	1.45	0	2.22	0
⋮	⋮	⋮	⋮	⋮	⋮	⋮	⋮	⋮	⋮	⋮
70	1.73	±72.1	1.41	±79.8	–	–	1.383	0	1.585	0
90	2.56	±71.6	2.10	±73.8	1.80	±86.6	–	–	1.85	0
120	4.15	±71.8	3.48	±71.8	2.97	±74.4	2.61	±85.5	2.28	±147.3

Table 8
Discontinuous intervals of $p_\gamma \times 10^{10}$ (V/m) for S_{min} as k_σ varies for Problem IV

Biaxial strain factor $k_\sigma = \sigma_{11}^\infty/\sigma_{33}^\infty$				
−1.0	−0.5	0	0.5	1.0
[−0.48, −0.37] [0.14, 0.21]	[−0.45, −0.31] [0.36, 0.45]	[−0.42, −0.24] [0.58, 0.70]	[−0.39, −0.18] [0.81, 0.95]	[−0.36,−0.11] [1.03, 1.20]

would require a knowledge of five independent mechanical and electrical components (σ_{11}^{∞}, σ_{33}^{∞}, σ_{31}^{∞}, D_1^{∞}, D_3^{∞}) whereby the remainders γ_{11}^{∞}, E_1^{∞}, etc. are dependent quantities.

A restriction of the asymptotic solutions given by Eqs. (8), (10), (15) and (17) is that S is only a function of θ. Note that $\mathrm{d}W/\mathrm{d}V$ in Eq. (5) is proportional to $1/r$ regardless of the boundary conditions. The crack initiation behavior predicted from the energy density factor $S_{\min}^{\max}$ applies only within a region close to the crack tip. Such a mathematical constraint may or may not confide with the physics of piezoelectricity where the electromechanical interaction of crack initiation may extend beyond the local region limited by the asymptotic expansion in Eq. (5). More specifically, the higher order term in r for $\mathrm{d}W/\mathrm{d}V$ may come into play. This is reminiscence of the earlier discussions concerned with the crack initiation path emanating from a narrow elliptical cavity [28–30]. Contrary to physical intuition, a noticeable "wiggle" was found in the crack profile close to the cavity boundary that is detectable by experiments. Such details would have escaped the attention of the investigators if the phenomenon was not first predicted by application of the full solution of $\mathrm{d}W/\mathrm{d}V$. It is in this spirit that the full solution of $\mathrm{d}W/\mathrm{d}V$ will be applied in an attempt to show that the peculiarities associated with $S_{\min}$ are caused by the approximate nature of the asymptotic solution and not by the energy density criterion. Each of the five boundary conditions will again be discussed to illustrate that the results in piezoelectricity are case specific. Generalization from limited examples and/or experimental data may not hold.

5.1. Energy density function in two dimensions

General application of the asymptotic solution in general is based on the assumption that there exists a region in which damage is localized. The distance of this region from the crack tip is for small r such that Eq. (5) for $\mathrm{d}W/\mathrm{d}V$ is valid. No attempts were made to address the change in r for different boundary conditions and material microstructures. On physical grounds, inhomogeneity and anisotropy would prevail ahead of the crack. This would give rise to a field of non-uniform energy states, the amplitude of which would oscillate as a function of the space variables. A multitude of peaks and valleys could be found; they are expressible mathematically as the maxima and minima of the energy density functions $\mathrm{d}W/\mathrm{d}V$. These locations are associated with damage by distortion and dilatation at a given scale [26,27]. Referred to a system of local polar cylindrical coordinates (r,θ) as shown in Fig. 1, the full field solution for $\mathrm{d}W/\mathrm{d}V$ can be computed and plotted as a function of r and θ. There will be a unique pair $[(\mathrm{d}W/\mathrm{d}V)_{\min}^{\max}, (\mathrm{d}W/\mathrm{d}V)_{\max}^{\max}]$ that would coincide with the behavior of damage initiation at two different scale levels; one of which respond linearily while the other non-linearily. A common example would be elastic fracture and plastic fracture. Such an interpretation can be applied to any two scale levels: atomic/micro, micro/meso, meso/macro and so on. The inhomogeneous character of damage must necessarily involve the specification of a distance, say r with reference to the half crack length a. In a specific problem, this would involve finding the stationary values of $\mathrm{d}W/\mathrm{d}V$ with r/a fixed and then vary θ from $-\pi$ to π. This would yield the predicted sites of damage initiation. The accuracy would depend on the chosen scale and depicted mesh size that would in turn depend on the prevailing boundary conditions and material parameters.

5.2. Location dependent damage

To reiterate is that predictions based on the energy density factor S in Eq. (5) could be referred to as being location independent, i.e., it does not specify the distance from which damage initiates. It only refers to the limit r approaching zero, i.e., the crack tip. As before, four boundary conditions will be considered. Each of them will specify the parameters p_σ, q_γ, q_σ and p_γ that stand for $E_3^{\infty}/\sigma_{33}^{\infty}$, $D_3^{\infty}/\gamma_{33}^{\infty}$, $D_3^{\infty}/\sigma_{33}^{\infty}$ and $E_3^{\infty}/\gamma_{33}^{\infty}$, respectively. The corresponding $\mathrm{d}W/\mathrm{d}V$ will be normalized to their values at infinity that would vary with p and q such that $k_\sigma = \sigma_{11}^{\infty}/\sigma_{33}^{\infty} = 0$ and $k_\gamma = \gamma_{11}^{\infty}/\gamma_{33}^{\infty} = 0$. They

are denoted as $(\mathrm{d}W/\mathrm{d}V)_{\mathrm{I}}^{\infty},\ldots,(\mathrm{d}W/\mathrm{d}V)_{\mathrm{IV}}^{\infty}$ and given by

- *Problem I*:

$$(\mathrm{d}W/\mathrm{d}V)_{\mathrm{I}}^{\infty}=\frac{(\sigma_{33}^{\infty})^2}{2}\left\{a_{33}+\frac{(p_\sigma+b_{33})^2}{d_{33}}\right\} \tag{20}$$

- *Problem II*:

$$(\mathrm{d}W/\mathrm{d}V)_{\mathrm{II}}^{\infty}=\frac{\gamma_{33}^2}{2}\left[\frac{(1-b_{33}q_\gamma)^2}{a_{33}}+d_{33}q_\gamma^2\right] \tag{21}$$

- *Problem III*:

$$(\mathrm{d}W/\mathrm{d}V)_{\mathrm{III}}^{\infty}=\frac{\sigma_{33}^2}{2}\left[\frac{(1-\mathrm{b}_{33}q_\varepsilon)^2}{\mathrm{a}_{33}}+d_{33}q_\sigma^2\right] \tag{22}$$

- *Problem IV*:

$$(\mathrm{d}W/\mathrm{d}V)_{\mathrm{IV}}^{\infty}=\frac{\gamma_{33}^2}{2}(c_{33}+\in_{33}p_\gamma^2) \tag{23}$$

In what follows, $\mathrm{d}W/\mathrm{d}V$ will be normalized in terms of $(\mathrm{d}W/\mathrm{d}V)_{\mathrm{I}}^{\infty}$, $(\mathrm{d}W/\mathrm{d}V)_{\mathrm{II}}^{\infty}$, etc. that are stated, respectively, in Eqs. (20) and (21), etc. The notation $(\mathrm{d}W/\mathrm{d}V)^{*}=(\mathrm{d}W/\mathrm{d}V)/(\mathrm{d}W/\mathrm{d}V)_{j}^{\infty}$ with $j=\mathrm{I}$, II, etc will be used. To avoid a lengthy mathematical disposition, presentation will be directed to those situations where the peculiarities of the asymptotic solution would not arise if the full field solution were used in conjunction with the energy density criterion. When electromechanical effects are present, damage ahead of a crack becomes location dependent. It is then necessary to address crack initiation behavior by two space variable even for mode I loading.

5.3. Specification of electric field and remote stress

Let $p_\sigma=E_3^{\infty}/\sigma_{33}^{\infty}$ be specified as in Problem I stated by Eq. (20) where the biaxial stress factor $k_\sigma=\sigma_{11}^{\infty}/\sigma_{33}^{\infty}$ can take different values. Recall from the results in Table 2 and Fig. 3 that the S^{*} against p_σ curves contain discontinuous intervals within which no stationary values of the energy density factor S could be found. The first reaction would be to cast doubt on the validity of the S-criterion which in retrospect would not have led to a better understanding of the problem. Instead, the discontinuous intervals of p_σ become non-existent when the full solution $\mathrm{d}W/\mathrm{d}V$ is used for different ratios of r/a that was not considered in the treatment of S. That is the form of Eq. (5) excluded the potential damage initiation sites that might have fallen outside the local region of asymptotic expansion. This is precisely what has happened when the full field solution of $\mathrm{d}W/\mathrm{d}V$ is used. Minima of $\mathrm{d}W/\mathrm{d}V$ were found for all values of p_σ and k_σ in Table 2. The relative distance r/a was required to address the precise location of damage initiated due to dilatation. Keep in mind that relative minimum of $\mathrm{d}W/\mathrm{d}V$ or $(\mathrm{d}W/\mathrm{d}V)_{\min}$ corresponds to location where volume change attains a minumum or dilatation is dominant. A more complete description of the damage initiation behavior can be obtained from the numerical values of $(\mathrm{d}W/\mathrm{d}V)_{\min}$ for a range of r/a, say 10^{-1}, 10^{-2}, 10^{-3} and 10^{-4}. They are given in Tables 9–12 inclusive. The column deleted contain data that are not so different from those shown.

Table 9
Predicted $(\mathrm{d}W/\mathrm{d}V)^{*}$ on crack initiation angles at $r/a=10^{-1}$ for Problem I

$p_\sigma\times10^{-3}$ (V m/N)	Biaxial stress factor $k_\sigma=\sigma_{11}^{\infty}/\sigma_{33}^{\infty}$									
	−0.90		−0.45		0		0.45		0.90	
	$(\mathrm{d}W/\mathrm{d}V)^{*}$ (×10)	θ_{o} (deg.)	$(\mathrm{d}W/\mathrm{d}V)^{*}$ (×10)	θ_{o} (deg.)	$(\mathrm{d}W/\mathrm{d}V)^{*}$ (×10)	θ_{o} (deg.)	$(\mathrm{d}W/\mathrm{d}V)^{*}$ (×10)	θ_{o} (deg.)	$(\mathrm{d}W/\mathrm{d}V)^{*}$ (×10)	θ_{o} (deg.)
−90	0.36	0.0	0.40	±109.8	0.48	±100.7	0.56	±95.0	0.67	±92.1
−70	0.33	±131.5	0.43	0.0	0.50	±108.2	0.61	±95.5	0.75	±89.4
−50	0.30	0.0	0.41	0.0	0.59	0.0	0.69	±106.9	0.86	±89.6
⋮	⋮	⋮	⋮	⋮	⋮	⋮	⋮	⋮	⋮	⋮
0	0.96	0.0	0.73	0.0	0.58	0.0	0.50	0.0	0.51	0.0
⋮	⋮	⋮	⋮	⋮	⋮	⋮	⋮	⋮	⋮	⋮
60	0.78	0.0	0.67	0.0	0.57	0.0	0.49	0.0	0.42	0.0

Table 10
Predicted $(dW/dV)^*$ on crack initiation angles at $r/a = 10^{-2}$ for Problem I

$p_\sigma \times 10^{-3}$ (V m/N)	Biaxial stress factor $k_\sigma = \sigma_{11}^\infty/\sigma_{33}^\infty$									
	−0.90		−0.45		0		0.45		0.90	
	$(dW/dV)^*$ (×10)	θ_o (deg.)	$(dW/dV)^*$ (×10)	θ_o (deg.)	$(dW/dV)^*$ (×10)	θ_o (deg.)	$(dW/dV)^*$ (×10)	θ_o (deg.)	$(dW/dV)^*$ (×10)	θ_o (deg.)
−90	0.32	±76.5	0.39	±74.3	0.47	±73.6	0.56	±73.4	0.67	±73.5
−70	0.34	0.0	0.40	±82.2	0.50	±76.5	0.61	±74.4	0.75	±73.6
−50	0.39	0.0	0.49	0.0	0.56	±93.7	0.70	±81.3	0.87	±76.6
⋮	⋮	⋮	⋮	⋮	⋮	⋮	⋮	⋮	⋮	⋮
0	0.95	0.0	0.76	0.0	0.63	0.0	0.54	0.0	0.51	0.0
⋮	⋮	⋮	⋮	⋮	⋮	⋮	⋮	⋮	⋮	⋮
60	0.71	0.0	0.61	0.0	0.52	0.0	0.45	0.0	0.38	0.0

Table 11
Predicted $(dW/dV)^*$ on crack initiation angles at $r/a = 10^{-3}$ for Problem I

$p_\sigma \times 10^{-3}$ (V m/N)	Biaxial stress factor $k_\sigma = \sigma_{11}^\infty/\sigma_{33}^\infty$									
	−0.90		−0.45		0		0.45		0.90	
	$(dW/dV)^*$ (×10^3)	θ_o (deg.)	$(dW/dV)^*$ (×10^3)	θ_o (deg.)	$(dW/dV)^*$ (×10^3)	θ_o (deg.)	$(dW/dV)^*$ (×10^3)	θ_o (deg.)	$(dW/dV)^*$ (×10^3)	θ_o (deg.)
−90	0.31	±73.6	0.38	±72.5	0.47	±72.0	0.56	±71.8	0.67	±71.8
−70	0.31	±82.8	0.39	±77.2	0.49	±74.4	0.61	±73.0	0.75	±72.2
−50	0.47	0.0	0.45	±99.0	0.56	±85.2	0.70	±78.6	0.87	±75.3
⋮	⋮	⋮	⋮	⋮	⋮	⋮	⋮	⋮	⋮	⋮
0	1.03	0.0	0.83	0.0	0.68	0.0	0.58	0.0	0.52	0.0
⋮	⋮	⋮	⋮	⋮	⋮	⋮	⋮	⋮	⋮	⋮
60	0.71	0.0	0.61	0.0	0.53	0.0	0.45	0.0	0.38	0.0

Table 12
Predicted $(dW/dV)^*$ on crack initiation angles at $r/a = 10^{-4}$ for Problem I

$p_\sigma \times 10^{-3}$ (V m/N)	Biaxial stress factor $k_\sigma = \sigma_{11}^\infty/\sigma_{33}^\infty$									
	−0.90		−0.45		0		0.45		0.90	
	$(dW/dV)^*$ (×10^4)	θ_o (deg.)	$(dW/dV)^*$ (×10^4)	θ_o (deg.)	$(dW/dV)^*$ (×10^4)	θ_o (deg.)	$(dW/dV)^*$ (×10^4)	θ_o (deg.)	$(dW/dV)^*$ (×10^4)	θ_o (deg.)
−90	0.31	±73.4	0.38	±72.3	0.47	±71.8	0.56	±71.6	0.67	±71.7
−70	0.31	±80.8	0.39	±76.5	0.49	±74.1	0.61	±72.7	0.75	±72.1
−50	0.36	±118.2	0.45	±94.0	0.56	±83.6	0.70	±78.1	0.87	±75.1
⋮	⋮	⋮	⋮	⋮	⋮	⋮	⋮	⋮	⋮	⋮
0	1.06	0.0	0.85	0.0	0.70	0.0	0.59	0.0	0.53	0.0
⋮	⋮	⋮	⋮	⋮	⋮	⋮	⋮	⋮	⋮	⋮
60	0.71	0.0	0.62	0.0	0.53	0.0	0.45	0.0	0.38	0.0

Dilatation dominant: To reiterate, tabulated will be the maximum of $(dW/dV)_{min}$ or $(dW/dV)_{min}^{max}$. In normalized form, it is written as $(dW/dV)^*$. Its location is given by r/a and θ_o. The dominant mode of energy release would be "dilatation" in contrast to "distortion" where dW/dV attains a

relative maximum because the change of volume is the smallest. Referring to Table 9 for $r/a = 10^{-1}$, p_σ is increased from -90 to 60 V m/N and k_σ is increased from -0.90 to 0.90. The predicted angles of crack initiation is θ_o while values of $(dW/dV)^*$ are also tabulated. Of significance is that the regions dominated by dilatation and distortion are sorted out automatically from the stationary values of dW/dV. No a priori knowledge of the location of crack and/or yielding initiation is required.

Energy density variations: Energy density is generally known to intensify with increasing magnitude of applied mechanical stress. Such a trend cannot be carried over directly to the presence of electric field since the poling direction could either elevate or lower the crack tip energy density. The degree of biaxiality controlled by the factor k_σ also interacts with the electric field. Note from the results in Tables 9–12 that $(dW/dV)^*$ would increase in general as p_σ and k_σ are increased. At $k_\sigma = 0.90$, $(dW/dV)^*$ decreases for increasing p_σ (negative). When the electric field becomes positive, $(dW/dV)^*$ would increase for increasing p_σ (positive). Hence, the applied electric field could either elevate or lower the crack front energy density field depending on whether the electric field is negative or positive. This can be easily seen from the data in Tables 12 and 13 for $k_\sigma = 0.90$.

Bifurcation: Displayed in Figs. 7 and 8 are constant $(dW/dV)^*$ contours around the crack tips at $r/a = 0$ for $k_\sigma = 0$ and $p_\sigma = -25 \times 10^{-3}$ and 25×10^{-3} V m/N, respectively. The contours are symmetric about x-axis; their amplitude tends to increase as the distance to the crack tip is decreased while the shape will not lean forward as much. Increase in transversely applied tension tends to reduce the crack opening distance. This encourages bifurcation when the electric field opposes poling, i.e., negative p_σ. Refer to the results

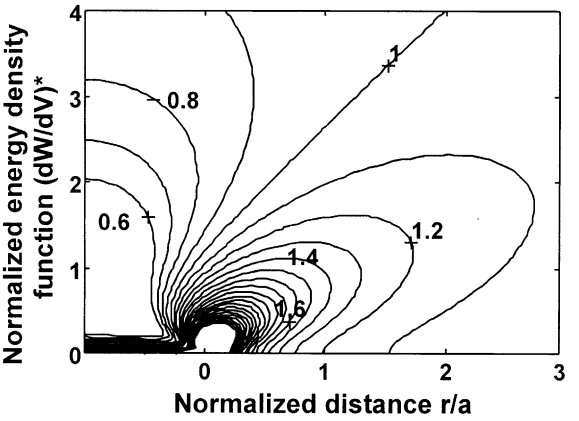

Fig. 7. Normalized energy density function verus distance with $p_\sigma = -25 \times 10^{-3}$ V m/N and $k_\sigma = 0$ for Problem I.

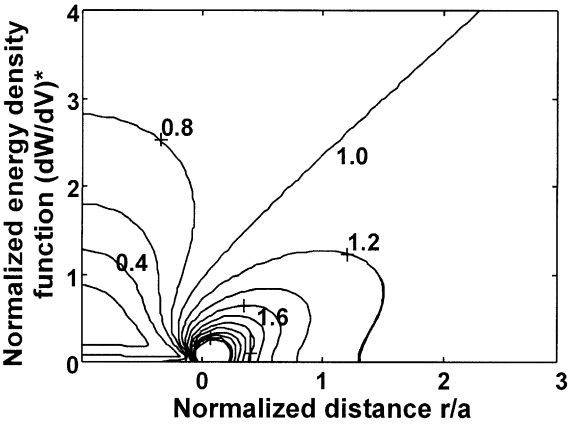

Fig. 8. Normalized energy density function verus distance with $p_\sigma = 25 \times 10^{-3}$ V m/N and $k_\sigma = 0$ for Problem I.

in Table 9 for $r/a = 10^{-1}$. Such a situation involves retardation of crack growth [19,20]. The branching angles increase with $(dW/dV)^*$ until the electric field becomes positive and a single branch crack path $\theta_o = 0°$ is predicted. Testing of a

Table 13
Variations of $(dW/dV)/(\sigma_{33}^\infty)^2$ and $(S/r)/(\sigma_{33}^\infty)^2$ for Problem I with $p_\sigma = 50 \times 10^{-3}$ V m/N and $k_\sigma = 0.90$

	Normalized distance r/a							
	0.002	0.008	0.01	0.012	0.02	0.1	0.5	1.0
$(dW/dV)/(\sigma_{33}^\infty)^2 \times 10^{-10}$	58.1	14.5	11.6	9.74	5.90	1.29	0.390	0.230
$(S/r)\sigma_{33}^\infty)^2 \times 10^{-10}$	58.3	14.6	11.6	9.73	5.80	1.17	0.287	0.117

stationary crack due to dilatation in isotropic elasticity is being predicted for the first time. It is seen from the results in Tables 9–12 that bifurcation seems to be associated with the decrease in $(dW/dV)^*$ as k_σ is increased from 0 to 0.90 while the applied electric field is negative. As soon as p_σ becomes positive, bifurcation ceases to occur and the crack is predicted to initiate straight ahead at $\theta_o = 0°$.

Multiscaling: It appears that when both electrical and mechanical disturbances are present as in a piezoelectric material, damage tends to depend on the distance from the crack expressed by the ratio r/a such that the size effect is reflected only in a relative sense. The actual distance r is not specified unless the crack size is known. While $r/a = 10^{-4}$ is small, the crack size a could still be large enough to give a value of r greater than that corresponding to $r/a = 10^{-3}$ where a is sufficiently small. This implies that unless the crack scale size such as microscopic, mesoscopic or macroscopic is specified, no specific information could be drawn on the actual magnitude of r from the data in Tables 9–12.

Nevertheless, the piezoelastic solution presented seems to yield a local damage behavior pattern associated with cracking modeled at the atomistic or microscopic scale. The works in [31,32] suggest a molecular dynamics region surrounding the crack tip at which bifurcation is assumed to model the emission of dislocations (refer to Fig. 9). The physical interpretation would differ in that forking is due to dilatation rather than shear as invoked in the dislocation model [31,32]. Furthermore, the region directly ahead of the microcrack experiences distortion. At the higher scale level, say macroscopic, the situation would be reversed. Distortion would correspond to the plastic enclaves at both sides of the macrocrack that is predicted to extend straight ahead along the path where dW/dV attain a minimum. The locations of $(dW/dV)_{min}$ and $(dW/dV)_{max}$ would also depend on the scales at which the damage is being modelled. Such a scenario of multiscale cracking was presented in [33].

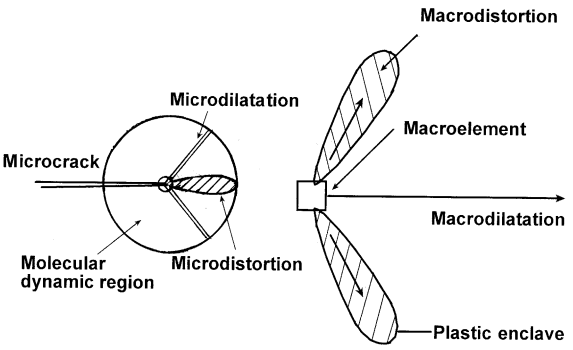

Fig. 9. Multiscale character near crack tip at micro- and macro-scale.

6. Inadequacy of asymptotic expansion for multiscale problems

When analyzing multiscale damage in a single formulation, the difference between the asymptotic and full field solution could be significant as they may lead to different conclusions. Three typical cases will be selected to illustrate why the full field solution should be used when the material response to electrical/mechanical effects depends on r/a in piezoelasticity. With reference to Problem I where the full field solution depends on $p_\sigma (= E_3^\infty/\sigma_{33}^\infty)$ and $k_\sigma (= \sigma_{11}^\infty/\sigma_{33}^\infty)$, Tables 13–15 show that the distance dependent character of the full solution dW/dV in addition to the electrical/mechanical boundary conditions for Problem I. For each of the three cases in Tables 13–15, the asymptotic

Table 14
Variations of $(dW/dV)/(\sigma_{33}^\infty)^2$ and $(S/r)/(\sigma_{33}^\infty)^2$ for Problem I with $p_\sigma = -50 \times 10^{-3}$ V m/N and $k_\sigma = 0$

	Normalized distance r/a							
	0.002	0.01	0.1	0.2	0.3	0.4	0.50	1.0
$(dW/dV)/(\sigma_{33}^\infty) \times 10^{-10}$	25.2	4.74	0.432	0.230	0.168	0.139	0.122	0.0927
$(S/r)/(\sigma_{33}^\infty)^2 \times 10^{-10}$	26.8	5.36	0.536	0.268	0.178	0.134	0.107	0.0536

Table 15
Variations of $(\mathrm{d}W/\mathrm{d}V)/(\sigma_{33}^{\infty})^2$ and $(S/r)/(\sigma_{33}^{\infty})^2$ for Problem I with $p_\sigma = 0$ and $k_\sigma = 1.8$

	Normalized distance r/a							
	0.002	0.01	0.1	0.2	0.4	0.6	0.8	1.0
$(\mathrm{d}W/\mathrm{d}V)/(\sigma_{33}^{\infty})^2 \times 10^{-10}$	19.2	4.02	0.517	0.312	0.207	0.173	0.156	0.146
$(S/r)/(\sigma_{33}^{\infty})^2 \times 10^{-10}$	18.6	3.72	0.372	0.186	0.093	0.062	0.0465	0.0372

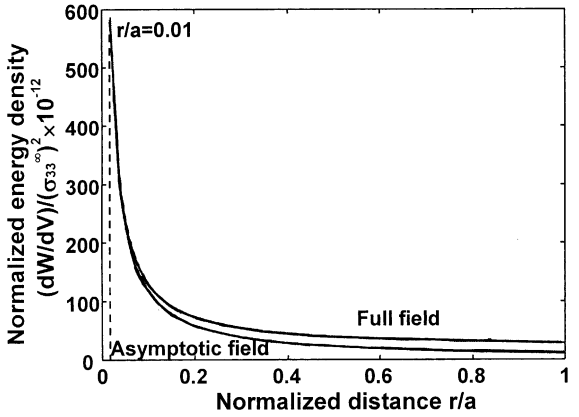

Fig. 10. Comparison of asymptotic and full field solution for $p_\sigma = 50 \times 10^{-3}$ V m/N and $k_\sigma = 0.90$.

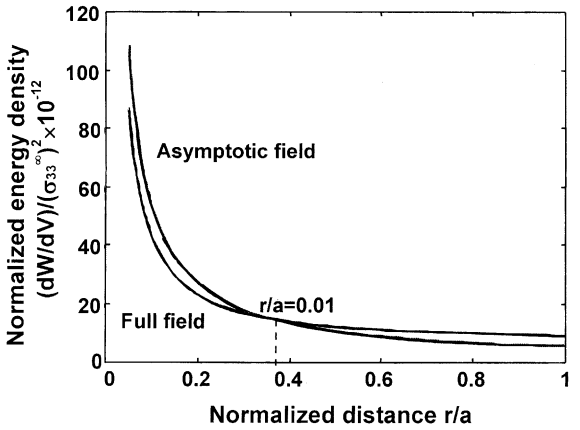

Fig. 11. Comparison of asymptotic and full field solution for $p_\sigma = -50 \times 10^{-3}$ V m/N and $k_\sigma = 0$.

solution S/r in Eq. (5) is also plotted to show how it differs with the full field solution $\mathrm{d}W/\mathrm{d}V$ as a function of the normalized distance r/a. As it should, the two solutions would converge as $r \to 0$ and diverge as r increases. Displayed in Fig. 10 are the results for $p_\sigma = 50 \times 10^{-3}$ V m/N and $k_\sigma = 0.90$ where the S/r and $\mathrm{d}W/\mathrm{d}V$ curves would intersect at a relatively small ratio of $r/a = 0.01$ and $(\mathrm{d}W/\mathrm{d}V)/(\sigma_{33}^{\infty})^2 = 0.116 \times 10^{-8}$ MPa. The inexactness of S/r therefore depends on the relative distance r/a. When p_σ is changed to -50×10^{-3} V m/N and the biaxial stress factor k_σ is reduced to zero, Fig. 11 shows that the intersection would occur for larger values of $r/a = 0.37$ and lower $\mathrm{d}W/\mathrm{d}V/(\sigma_{33}^{\infty})^2$ of 0.146×10^{-10} MPa. The discrepancies between S/r and $\mathrm{d}W/\mathrm{d}V$ are sensitive to changes in p_σ and k_σ. This again reinforces the need to use the full field solution such that damage along the line of prospective crack extension would be included. For the third case in Table 15 and Fig. 12, the curves would not intersect but they do diverge for large r/a.

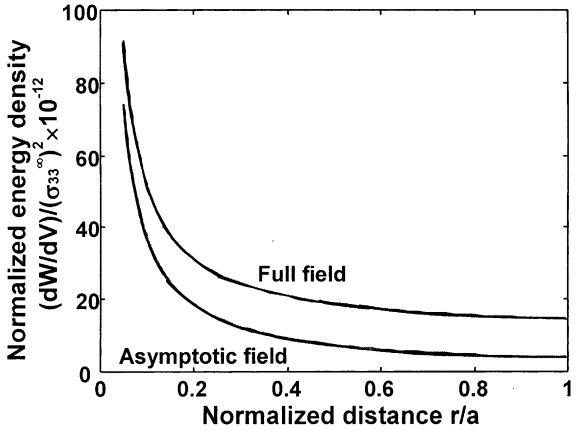

Fig. 12. Comparison of asymptotic and full field solution for $p_\sigma = 0$ and $k_\sigma = 1.8$.

Worthy of mentioning is also the monotonic behavior of the $\mathrm{d}W/\mathrm{d}V$ and S/r curves in Figs. 10–12. No stationary values are predicted in terms of the variable r. According to the interpretation of the energy density criterion, there is no damage

preference in terms of the distance from the crack tips because the boundaries extend to infinity. Hence, both S/r and dW/dV tend to decay monotonically with r/a.

In general, however, dW/dV is a function of both r and θ for two-dimensional problems, Many maxima and minima of dW/dV could be found. Yield and fracture initiation sites are unique. They correspond to the maximum of $(dW/dV)_{max}$ for the onset of yielding and $(dW/dV)_{min}$ for the onset of fracturing. Some examples for isotropic elastic materials can be found in [27].

7. Influence of boundary conditions on scaling

Molecular dynamics simulations [34,35] have shown that the length and time scales at the atomic level are significantly different than those at the continuum level although no direct relationships have been established. While the ab initio damage of solids is presently taken at the atomic level, it is not clear how the events at 10^{-8} cm in lineal dimension are related to those at 10^{-2} or 10^{-3} cm in lineal dimension. In practical terms, it is important to know the conditions under which atomistic effects would influence the macroscopic behavior. Even more relevant is how this process could be modeled with consistency in a numerical analysis that may involve the sliding of atomic planes [31,32] over each other or the breaking of cohesive bonds [36] between the atoms. At present, the atomic damage mechanisms are anticipated independent of the macroscopic failure criteria. One of such assumptions that has been taken for granted is the relation between edge dislocations with a mode II macrocrack behavior. More recent results based on molecular dynamics [37,38] show that they are very different, particularly for moving cracks.

Too much emphases cannot be placed on relating the atomic (or microscopic) and macroscopic behavior should such connections prevail. Indeed the results in Tables 9–12 inclusive for $r/a = 10^{-1}$ to 10^{-4} suggest that such possibilities do exist and they depend on the boundary conditions identified with Problems I–IV by Eqs. (8)–(19) inclusive. In this respect, continuum mechanics could serve a useful purpose. It does not address scaling. Hence, it can be applied to the atomic as well as the macroscopic scale and can provide an indication of how boundary conditions could affect the end results. Recall the two different crack tip behavior in Fig. 9. They do not always appear as a rule but depend on the biaxial stress and strain factors in addition to the relative amplitudes of the applied electric field, electric displacement, mechanical stress and strain. Hence, no conclusions could be drawn from the results for one specific set of boundary conditions. To this end, bifurcation data for Problems II–IV will also be examined using the full field solution and the energy density criterion. Keep in mind that dW/dV or $(dW/dV)^*$ from the crack tip may not follow $1/r$; it may be some function of r.

7.1. Electric displacement and mechanical strain

Suppose that D_3^∞ and γ_{33}^∞ are specified as a ratio via q_γ following the conditions specified in Eqs. (10)–(14). In order to exhibit the bifurcation feature the range of q_γ (C/m^2) is selected from -50 to 70. The values of $(dW/dV)^*$ for different r/a from 10^{-1} to 10^{-4} and biaxial strain factor k_γ can be found in Tables 16–19.

Unlike the case for Problem I and results in Tables 9–12, Table 16 for $r/a = 10^{-1}$ shows that bifurcation appears only for $k_\gamma = -0.90$ and $q_\gamma = -50$ and -40 C/m^2 and large values of positive q_γ. Otherwise, crack growth is predicted to occur straight ahead. This situation changes for $r/a < 10^{-2}$ where bifurcation occurs for all k_γ as shown in Tables 18 and 19 when q_γ equals to -50 and -40 C/m^2. As q_γ becomes positive, bifurcation does not occur until it passes beyond 50 C/m^2 as k_γ becomes larger than -0.45. This behavior is also very different from that for Problem I where the biaxial stress factor is specified instead of the biaxial strain factor.

7.2. Electric displacement and mechanical stress

Now, if mechanical stress σ_{33}^∞ is specified with the electric displacement E_3^∞ via k_σ further difference in bifurcation will be found. Refer to the data in Tables 20–23 as r/a is varied from 10^{-1} to 10^{-4}, respectively for Problem III. Note that

Table 16
Predicted $(dW/dV)^*$ on crack initiation angles at $r/a = 10^{-1}$ for Problem II

q_γ (C/m^2)	Biaxial strain factor $k_\gamma = \gamma_{11}^\infty/\gamma_{33}^\infty$									
	−0.90		−0.45		0		0.45		0.90	
	$(dW/dV)^*$ ($\times 10^1$)	θ_o (deg.)	$(dW/dV)^*$ ($\times 10^1$)	θ_o (deg.)	$(dW/dV)^*$ ($\times 10^1$)	θ_o (deg.)	$(dW/dV)^*$ ($\times 10^1$)	θ_o (deg.)	$(dW/dV)^*$ ($\times 10^1$)	θ_o (deg.)
−50	0.40	±135.2	0.48	0.0	0.57	0.0	0.69	0.0	0.83	0.0
−40	0.39	±136.7	0.48	0.0	0.60	0.0	0.75	0.0	0.92	0.0
⋮	⋮	⋮	⋮	⋮	⋮	⋮	⋮	⋮	⋮	⋮
0	0.25	0.0	0.46	0.0	0.79	0.0	1.24	0.0	1.82	0.0
10	0.22	0.0	0.43	0.0	0.79	0.0	1.31	0.0	1.99	0.0
⋮	⋮	⋮	⋮	⋮	⋮	⋮	⋮	⋮	⋮	⋮
60	0.34	±101.2	0.33	±113.5	0.33	±133.0	–	–	–	–
70	0.36	±101.2	0.35	±109.5	0.34	±118.7	0.35	±134.8	–	–

Table 17
Predicted $(dW/dV)^*$ on crack initiation angles at $r/a = 10^{-2}$ for Problem II

q_γ (C/m^2)	Biaxial strain factor $k_\gamma = \gamma_{11}^\infty/\gamma_{33}^\infty$									
	−0.90		−0.45		0		0.45		0.90	
	$(dW/dV)^*$ ($\times 10^2$)	θ_o (deg.)	$(dW/dV)^*$ ($\times 10^2$)	θ_o (deg.)	$(dW/dV)^*$ ($\times 10^2$)	θ_o (deg.)	$(dW/dV)^*$ ($\times 10^2$)	θ_o (deg.)	$(dW/dV)^*$ ($\times 10^2$)	θ_o (deg.)
−50	0.47	0.0	0.56	0.0	0.67	0.0	0.65	±112.6	0.74	±113.3
−40	0.46	0.0	0.57	0.0	0.70	0.0	0.85	0.0	0.79	±118.8
⋮	⋮	⋮	⋮	⋮	⋮	⋮	⋮	⋮	⋮	⋮
0	0.33	0.0	0.58	0.0	0.91	0.0	1.32	0.0	1.80	0.0
10	0.27	0.0	0.52	0.0	0.86	0.0	1.31	0.0	1.85	0.0
⋮	⋮	⋮	⋮	⋮	⋮	⋮	⋮	⋮	⋮	⋮
60	0.34	±75.0	0.32	±81.5	0.32	±97.5	–	–	–	–
70	0.36	±73.8	0.33	±76.6	0.32	±84.0	0.32	±98.2	–	–

Table 18
Predicted $(dW/dV)^*$ on crack initiation angles at $r/a = 10^{-3}$ for Problem II

q_γ (C/m^2)	Biaxial strain factor $k_\gamma = \gamma_{11}^\infty/\gamma_{33}^\infty$									
	−0.90		−0.45		0		0.45		0.90	
	$(dW/dV)^*$ ($\times 10^3$)	θ_o (deg.)	$(dW/dV)^*$ ($\times 10^3$)	θ_o (deg.)	$(dW/dV)^*$ ($\times 10^3$)	θ_o (deg.)	$(dW/dV)^*$ ($\times 10^3$)	θ_o (deg.)	$(dW/dV)^*$ ($\times 10^3$)	θ_o (deg.)
−50	0.43	±91.8	0.50	±94.5	0.58	±97.0	0.67	±99.4	0.76	±101.6
−40	0.42	±95.7	0.51	±98.8	0.60	±101.7	0.71	±104.3	0.82	±106.9
⋮	⋮	⋮	⋮	⋮	⋮	⋮	⋮	⋮	⋮	⋮
0	0.40	0.0	0.67	0.0	1.00	0.0	1.39	0.0	1.85	0.0
10	0.32	0.0	0.58	0.0	0.92	0.0	1.34	0.0	1.85	0.0
⋮	⋮	⋮	⋮	⋮	⋮	⋮	⋮	⋮	⋮	⋮
60	0.34	±72.7	0.32	±77.8	0.32	±93.3	–	–	–	–
70	0.36	±71.8	0.33	±73.6	0.32	±79.6	0.31	±94.0	–	–

bifurcation now occurs at large almost for all values of q_σ and k_σ except when $q_\sigma = 0$ and 10×10^{-11} C/N. The specification of both E_3^∞ and σ_{33}^∞ seems to favor crack forking in piezoelectric ceramic materials, a prediction that deserves experimental validation.

Table 19
Predicted $(dW/dV)^*$ on crack initiation angles at $r/a = 10^{-4}$ for Problem II

q_γ (C/m^2)	Biaxial strain factor $k_\gamma = \gamma_{11}^\infty/\gamma_{33}^\infty$									
	−0.90		−0.45		0		0.45		0.90	
	$(dW/dV)^*$ ($\times 10^4$)	θ_o (deg.)	$(dW/dV)^*$ ($\times 10^4$)	θ_o (deg.)	$(dW/dV)^*$ ($\times 10^4$)	θ_o (deg.)	$(dW/dV)^*$ ($\times 10^4$)	θ_o (deg.)	$(dW/dV)^*$ ($\times 10^4$)	θ_o (deg.)
−50	0.43	±88.0	0.50	±90.8	0.58	±93.4	0.67	±96.0	0.76	±98.4
−40	0.43	±91.0	0.51	±94.3	0.61	±97.5	0.71	±100.5	0.82	±103.3
⋮	⋮	⋮	⋮	⋮	⋮	⋮	⋮	⋮	⋮	⋮
0	0.43	0.0	0.70	0.0	1.03	0.0	1.42	0.0	1.87	0.0
10	0.34	0.0	0.60	0.0	0.94	0.0	1.36	0.0	1.86	0.0
⋮	⋮	⋮	⋮	⋮	⋮	⋮	⋮	⋮	⋮	⋮
60	0.34	±72.6	0.32	±77.4	0.32	±92.9	–	–	0.38	0.0
70	0.36	±71.7	0.33	±73.4	0.32	±79.0	0.31	±93.6	–	–

Table 20
Predicted $(dW/dV)^*$ on crack initiation angles at $r/a = 10^{-1}$ for Problem III

$q_\sigma \times 10^{-11}$ (C/N)	Biaxial stress factor $k_\sigma = \sigma_{11}^\infty/\sigma_{33}^\infty$									
	−0.90		−0.45		0.0		0.45		0.90	
	$(dW/dV)^*$ ($\times 10$)	θ_o (deg.)	$(dW/dV)^*$ ($\times 10$)	θ_o (deg.)	$(dW/dV)^*$ ($\times 10$)	θ_o (deg.)	$(dW/dV)^*$ ($\times 10$)	θ_o (deg.)	$(dW/dV)^*$ ($\times 10$)	θ_o (deg.)
−80	0.42	±125.6	0.42	±125.5	0.42	±125.4	0.42	±125.3	0.42	±125.2
⋮	⋮	⋮	⋮	⋮	⋮	⋮	⋮	⋮	⋮	⋮
−10	0.47	±106.9	0.46	±103.7	0.46	±100.5	0.45	±97.5	0.45	±94.8
0	0.49	0.0	0.52	0.0	0.58	0.0	0.69	0.0	0.84	0.0
10	0.57	0.0	0.57	0.0	0.57	0.0	0.58	0.0	0.59	0.0
100	0.40	±147.9	0.40	±148.0	0.40	±148.0	0.40	±148.1	0.40	±148.1

Table 21
Predicted $(dW/dV)^*$ on crack initiation angles at $r/a = 10^{-2}$ for Problem III

$q_\sigma \times 10^{-11}$ (C/N)	Biaxial stress factor $k_\sigma = \sigma_{11}^\infty/\sigma_{33}^\infty$									
	−0.90		−0.45		0.0		0.45		0.90	
	$(dW/dV)^*$ ($\times 10^2$)	θ_o (deg.)	$(dW/dV)^*$ ($\times 10^2$)	θ_o (deg.)	$(dW/dV)^*$ ($\times 10^2$)	θ_o (deg.)	$(dW/dV)^*$ ($\times 10^2$)	θ_o (deg.)	$(dW/dV)^*$ ($\times 10^2$)	θ_o (deg.)
−80	0.44	±93.7	0.44	±93.6	0.44	±93.6	0.44	±93.6	0.44	±93.6
⋮	⋮	⋮	⋮	⋮	⋮	⋮	⋮	⋮	⋮	⋮
−10	0.45	±74.6	0.45	±74.5	0.45	±74.4	0.45	±74.3	0.45	±74.2
0	0.65	0.0	0.69	0.0	0.74	0.0	0.79	0.0	0.84	0.0
10	0.51	0.0	0.52	0.0	0.52	0.0	0.52	0.0	0.53	0.0
⋮	⋮	⋮	⋮	⋮	⋮	⋮	⋮	⋮	⋮	⋮
100	0.44	±111.4	0.44	±111.4	0.44	±111.4	0.44	±111.4	0.44	111.3

7.3. Electric field and mechanical strain

This combination is similar to that Problem II in which the electric displacement is now replaced by electric field. The bifurcation behavior for Problem IV is also similar. That is the data in Tables 24–27 possess the same trend as that in Tables 16–19. For the most part, crack is predicted

Table 22
Predicted $(dW/dV)^*$ on crack initiation angles at $r/a = 10^{-3}$ for Problem III

$q_\sigma \times 10^{-11}$ (C/N)	Biaxial stress factor $k_\sigma = \sigma_{11}^\infty/\sigma_{33}^\infty$									
	−0.90		−0.45		0.0		0.45		0.90	
	$(dW/dV)^*$ ($\times 10^3$)	θ_o (deg.)	$(dW/dV)^*$ ($\times 10^3$)	θ_o (deg.)	$(dW/dV)^*$ ($\times 10^3$)	θ_o (deg.)	$(dW/dV)^*$ ($\times 10^3$)	θ_o (deg.)	$(dW/dV)^*$ ($\times 10^3$)	θ_o (deg.)
−80	0.44	±89.8	0.44	±89.8	0.44	±89.8	0.44	±89.8	0.44	±89.8
⋮	⋮	⋮	⋮	⋮	⋮	⋮	⋮	⋮	⋮	⋮
−10	0.45	±72.2	0.45	±72.2	0.45	±72.2	0.45	±72.2	0.45	±72.2
0	0.80	0.0	0.82	0.0	0.83	0.0	0.85	0.0	0.87	0.0
10	0.52	0.0	0.52	0.0	0.52	0.0	0.52	0.0	0.52	0.0
⋮	⋮	⋮	⋮	⋮	⋮	⋮	⋮	⋮	⋮	⋮
100	0.44	±106.4	0.44	±106.4	0.44	±106.4	0.44	±106.4	0.44	±106.4

Table 23
Predicted $(dW/dV)^*$ on crack initiation angles at $r/a = 10^{-4}$ for Problem III

$q_\sigma \times 10^{-11}$ (C/N)	Biaxial stress factor $k_\sigma = \sigma_{11}^\infty/\sigma_{33}^\infty$									
	−0.90		−0.45		0.0		0.45		0.90	
	$(dW/dV)^*$ ($\times 10^4$)	θ_o (deg.)	$(dW/dV)^*$ ($\times 10^4$)	θ_o (deg.)	$(dW/dV)^*$ ($\times 10^4$)	θ_o (deg.)	$(dW/dV)^*$ ($\times 10^4$)	θ_o (deg.)	$(dW/dV)^*$ ($\times 10^4$)	θ_o (deg.)
−80	0.44	±89.4	0.44	±89.4	0.44	±89.4	0.44	±89.4	0.44	±89.4
⋮	⋮	⋮	⋮	⋮	⋮	⋮	⋮	⋮	⋮	⋮
−10	0.45	±72.1	0.45	±72.1	0.45	±72.1	0.45	±72.1	0.45	±72.1
0	0.86	0.0	0.87	0.0	0.87	0.0	0.88	0.0	0.88	0.0
10	0.52	0.0	0.52	0.0	0.52	0.0	0.52	0.0	0.52	0.0
⋮	⋮	⋮	⋮	⋮	⋮	⋮	⋮	⋮	⋮	⋮
100	0.44	±105.8	0.44	±105.8	0.44	±105.8	0.44	±105.8	0.44	±105.8

Table 24
Predicted $(dW/dV)^*$ on crack initiation angles at $r/a = 10^{-1}$ for Problem IV

$p_\gamma \times 10^{-8}$ (V/m)	Biaxial strain factor $k_\gamma = \gamma_{11}^\infty/\gamma_{33}^\infty$									
	−1.0		−0.5		0		0.5		1.0	
	$(dW/dV)^*$ ($\times 10^1$)	θ_o (deg.)	$(dW/dV)^*$ ($\times 10^1$)	θ_o (deg.)	$(dW/dV)^*$ ($\times 10^1$)	θ_o (deg.)	$(dW/dV)^*$ ($\times 10^1$)	θ_o (deg.)	$(dW/dV)^*$ ($\times 10^1$)	θ_o (deg.)
−90	0.28	±138.7	0.41	0.0	0.61	0.0	0.86	0.0	1.17	0.0
⋮	⋮	⋮	⋮	⋮	⋮	⋮	⋮	⋮	⋮	⋮
−20	0.17	0.0	0.37	0.0	0.80	0.0	1.45	0.0	2.32	0.0
−10	0.21	0.0	0.38	0.0	0.80	0.0	1.47	0.0	2.40	0.0
0	0.28	0.0	0.39	0.0	0.77	0.0	1.41	0.0	2.31	0.0
10	0.37	0.0	0.41	0.0	0.70	0.0	1.25	0.0	–	–
⋮	⋮	⋮	⋮	⋮	⋮	⋮	⋮	⋮	⋮	⋮
120	0.46	±102.6	0.40	±108.0	0.35	±114.9	0.32	±126.7	–	–

to extend straight ahead with $\theta_o = 0$ for p_γ in the middle range. For small p_γ, say -90×10^{-8} V/m, bifurcation seems to depend on the biaxial factor k_γ. As p_γ becomes positive and increases, crack forking is predicted regardless of the biaxial strain factor k_γ. The interdependency of crack initiation

Table 25
Predicted $(dW/dV)^*$ on crack initiation angles at $r/a = 10^{-2}$ for Problem IV

$p_\gamma \times 10^{-8}$ (V/m)	Biaxial strain factor $k_\gamma = \gamma_{11}^\infty/\gamma_{33}^\infty$									
	−1.0		−0.5		0		0.5		1.0	
	$(dW/dV)^*$ ($\times 10^2$)	θ_o (deg.)	$(dW/dV)^*$ ($\times 10^2$)	θ_o (deg.)	$(dW/dV)^*$ ($\times 10^2$)	θ_o (deg.)	$(dW/dV)^*$ ($\times 10^2$)	θ_o (deg.)	$(dW/dV)^*$ ($\times 10^2$)	θ_o (deg.)
−90	0.33	0.0	0.50	0.0	0.72	0.0	0.98	0.0	1.00	117.6
⋮	⋮	⋮	⋮	⋮	⋮	⋮	⋮	⋮	⋮	⋮
−20	0.19	0.0	0.47	0.0	0.91	0.0	1.53	0.0	2.31	0.0
−10	0.21	0.0	0.45	0.0	0.88	0.0	1.51	0.0	2.32	0.0
0	0.25	0.0	0.43	0.0	0.80	0.0	1.38	0.0	2.16	0.0
10	0.32	0.0	0.41	0.0	0.69	0.0	1.17	0.0	1.84	0.0
⋮	⋮	⋮	⋮	⋮	⋮	⋮	⋮	⋮	⋮	⋮
120	0.45	±73.6	0.38	±74.1	0.33	±78.7	0.29	±91.2	–	–

Table 26
Predicted $(dW/dV)^*$ on crack initiation angles at $r/a = 10^{-3}$ for Problem IV

$p_\gamma \times 10^{-8}$ (V/m)	Biaxial strain factor $k_\gamma = \gamma_{11}^\infty/\gamma_{33}^\infty$									
	−1.0		−0.5		0		0.5		1.0	
	$(dW/dV)^*$ ($\times 10^3$)	θ_o (deg.)	$(dW/dV)^*$ ($\times 10^3$)	θ_o (deg.)	$(dW/dV)^*$ ($\times 10^3$)	θ_o (deg.)	$(dW/dV)^*$ ($\times 10^3$)	θ_o (deg.)	$(dW/dV)^*$ ($\times 10^3$)	θ_o (deg.)
−90	0.31	±102.4	0.45	±103.7	0.61	±104.6	0.81	±105.3	1.03	±106.0
⋮	⋮	⋮	⋮	⋮	⋮	⋮	⋮	⋮	⋮	⋮
−20	0.24	0.0	0.53	0.0	0.99	0.0	1.61	0.0	–	–
−10	0.24	0.0	0.50	0.0	0.94	0.0	1.57	0.0	2.37	0.0
0	0.27	0.0	0.46	0.0	0.84	0.0	1.42	0.0	2.18	0.0
10	0.32	0.0	0.43	0.0	0.71	0.0	1.18	0.0	1.83	0.0
⋮	⋮	⋮	⋮	⋮	⋮	⋮	⋮	⋮	⋮	⋮
120	0.45	±71.8	0.38	±72.0	0.32	±74.9	0.28	±86.3	–	–

Table 27
Predicted $(dW/dV)^*$ on crack initiation angles at $r/a = 10^{-4}$ for Problem IV

$p_\gamma \times 10^{-8}$ (V/m)	Biaxial strain factor $k_\gamma = \gamma_{11}^\infty/\gamma_{33}^\infty$									
	−1.0		−0.5		0		0.5		1.0	
	$(dW/dV)^*$ ($\times 10^4$)	θ_o (deg.)	$(dW/dV)^*$ ($\times 10^4$)	θ_o (deg.)	$(dW/dV)^*$ ($\times 10^4$)	θ_o (deg.)	$(dW/dV)^*$ ($\times 10^4$)	θ_o (deg.)	$(dW/dV)^*$ ($\times 10^4$)	θ_o (deg.)
−90	0.31	±95.8	0.45	±98.2	0.62	±100.0	0.81	±101.4	1.03	±102.6
⋮	⋮	⋮	⋮	⋮	⋮	⋮	⋮	⋮	⋮	⋮
−20	0.25	0.0	0.56	0.0	1.02	0.0	1.64	0.0	–	–
−10	0.25	0.0	0.52	0.0	0.97	0.0	1.59	0.0	2.39	0.0
0	0.27	0.0	0.47	0.0	0.86	0.0	1.43	0.0	2.19	0.0
10	0.32	0.0	0.43	0.0	0.72	0.0	1.19	0.0	1.83	0.0
⋮	⋮	⋮	⋮	⋮	⋮	⋮	⋮	⋮	⋮	⋮
120	0.45	±71.8	0.38	±71.8	0.32	±74.6	0.28	±85.6	0.25	±147.9

conditions with boundary conditions is not unexpected. However, the predicted branching for stationary cracks is new.

8. Conclusions

Atomistic simulation of crack tip behavior has motivated this work. Piezoelasticity solution has led to two different crack tip stress field characteristics when the relative length parameter r/a is varied in conjunction with the electrical/mechanical boundary conditions. This finding was not expected even though the material characteristics ahead of the crack are altered for the tetragonal perovskite structure ceramics when the electric field direction is changed with reference to that of poling. More specifically, the local stresses and displacements were expected to be more dependent on the distance from the crack tip for piezoceramics. The dual stress and/or strain field characteristic may not be limited to piezoelasticity. That is local damage owing to dilatation and distortion is distant dependent. This multiscale feature of crack front damage is subject to additional investigation.

For small values of r/a and appropriate boundary conditions, the energy density criterion predicted two planes off to the crack along which dilatation dominates in contrast to distortion directly ahead of the crack. More specifically, bifurcation is predicted for a mode I stationary crack. For large values of r/a, straight ahead cracking is predicted that coincides with the dominant phases of dilatation. Distortional dominant planes are off to the sides where the prospective plastic enclaves would be developed. These results tend to suggest two different mechanisms of damage initiation when the scale size of r is changed in relation to crack length. There is also the implication that the dominant mode of damage for crack bifurcation is dilatation and not distortion or shear as assumed in dislocation mechanics where two slip planes off to the sides of a mode I crack are assumed.

Recent findings from molecular dynamics on dislocations [37,38] have suggested a closer look at previous models that have regarded piled-up dislocations as continuous sheets of dislocations with infinitesimal Burgers vectors. Tensile and in-plane shear cracks were assumed to be deducible mathematically from dislocations using the traction-free conditions. Although the results appear plausible, it is difficult to justify the scale difference of several orders of magnitude. Different mechanisms of damage at the atomic scale may lead to similar macrocrack configurations. Uniqueness of this process may be invoked mathematically but it may prove to be impossible to show physically. There does not appear to be the sufficient conditions to model atomistic damage near the crack tip.

References

[1] Y.E. Pak, A. Tobin, On the electric field effects in fracture of piezoelectric materials, Mechanics of Electromagnetic Materials and Structures, AMD—vol. 161/MD—vol. 42, ASME, 1993.
[2] A. Tobin, Y.E. Pak, Effects if electric fields on fracture behavior of PZT ceramics, in: V.K. Varadan (Ed.), Smart Materials, SPIE vol. 1916, 1993, pp. 77–86.
[3] S. Park, C.T. Sun, Fracture criterion of piezoelectric ceramics, J. Am. Ceram. Soc. 78 (1995) 1475–1480.
[4] H.J. Gao, T.Y. Zhang, P. Tong, Local and global energy release rates for an electrically yielded crack in a piezoelectric ceramic, J. Mech. Phys. Solids 45 (1997) 491–510.
[5] W. Yang, Z. Suo, Cracking in ceramic actuators caused by electrostriction, J. Mech. Phys. Solids 42 (1994) 649–663.
[6] C.S. Lynch, W. Yang, L. Collier, Z. Suo, R.M. McMeeking, Electric field induced cracking in ferroelectric ceramics, J. Ferroelectrics 166 (1995) 11–30.
[7] T.H. Hao, X. Gong, Z. Suo, Fracture mechanics for the design of ceramic multilayer actuators, J. Mech. Phys. 44 (1996) 23–48.
[8] S.C. Hwang, C.S. Lynch, R.M. McMeeking, Ferroelectric/ferroelastic interactions and a polarization switching model, Acta Metall. Mater. 43 (5) (1995) 2073–2084.
[9] D.N. Fang, W. Lu, K.C. Hwang, Micromechanics of ferroelectric domain switching behavior: Part I—Coupled electromechanical field of domain inclusions, G.C. Sih, V.E. Panin (Eds.), Prospect of Mesomechanics in the 21st Century, J. Theor. Appl. Fract. Mech. 37 (2002) 29–38.
[10] D.N. Fang, W. Lu, K.C. Hwang, Micromechanics of ferroelectric domain switching behavior: Part II—Constitutive Relations and hysteresis, in: G.C. Sih, V.E. Panin (Eds.), Prospect of Mesomechanics in the 21st Century, J. Theor. Appl. Fract. Mech. 37 (2002) 39–47.
[11] Y.E. Pak, Crack extension forces in a piezoelectric material, J. Appl. Mech. 57 (1990) 647–653.

[12] Y.E. Pak, Linear electro-elastic fracture mechanics of piezoelectric materials, Int. J. Fract. 54 (1992) 79–100.
[13] Z. Suo, C.M. Kuo, D.M. Barnett, J.R. Willis, Fracture mechanics for piezoelectric ceramics, J. Mech. Phys. Solids 40 (1992) 739–765.
[14] H. Gao, D.M. Barnett, An invariance property of local energy release rates in a strip saturation model of piezoelectric fracture, Int. J. Fract. 79 (1996) R25–R29.
[15] Z. Suo, Model for breakdown-resistant dielectric and ferroelectric ceramics, J. Mech. Phys. Solids 41 (1993) 1155–1176.
[16] S. Shen, T. Nishioka, Fracture of piezoelectric materials: energy density criterion, J. Theor. Appl. Fract. Mech. 33 (1) (2000) 57–63.
[17] Z.T. Chen, Anti-plane mechanical and in-plane electric time-dependent load applied to two coplanar cracks in piezoelectric ceramic material, J. Theor. Appl. Fract. Mech. 33 (3) (2000) 173–184.
[18] B.L. Wang, N. Noda, Thermally induced fracture of a smart functionally graded composite structure, J. Theor. Appl. Fract. Mech. 35 (2) (2001) 93–109.
[19] J.Z. Zuo, G.C. Sih, Energy density formulation and interpretation of cracking behavior for piezoelectric ceramics, J. Theor. Appl. Fract. Mech. 34 (1) (2000) 17–33.
[20] G.C. Sih, J.Z. Zuo, Energy density formulation and interpretation of cracking behavior for piezoelectric ceramics, J. Theor. Appl. Fract. Mech. 34 (2) (2000) 123–141.
[21] A.K. Soh, D.N. Fang, K.L. Lee, Fracture criterion for piezoelectric materials with defects based on energy density theory, Proceedings of the 10th International Conference on Fracture, Hawaii, 2–6 December 2001, p. 755.
[22] G.C. Sih, Effect of electric field reversal on crack growth behavior of poled piezoelectric ceramic, Proceedings of the 10th International Congress on Fracture, Hawaii, 2–6 December 2001, p. 711.
[23] G.C. Sih, B. Liu, Z.F. Song, H.F. Ren, Anti-plane shear crack growth in piezoceramics: change of electric field and displacement direction, Proceedings of the 10th International Congress on Fracture, Hawaii, 2–6 December 2001, p. 714.
[24] G.C. Sih, Thermomechanics of solids: nonequilibrium and irreversibility, J. Theor. Appl. Fract. Mech. 9 (3) (1988) 175–198.
[25] G.C. Sih, Some Basic Problems in Nonequilibrium Thermomechanics, in: S. Sienietyez, P. Salamon, Tayler and Francis, New York, 1992, pp. 218–247.
[26] G.C. Sih (Ed.), Mechanics of Fracture, vols. I–VII, Noordhoff International Publishing, Leyden, 1973–1981.
[27] G.C. Sih, Mechanics of Fracture Initiation and Propagation, Kluwer Academic Publishers, The Netherlands, 1991.
[28] A.A. Griffith, The theory of rupture, Proceedings of the First International Congress of Applied Mathematics, Delft, 1924, pp. 55–93.
[29] F.A. McClintock, Discussion on crack extension in plates under plane loading and transverse shear, in: F. Erdogan, G.C. Sih (Eds.), J. Basic Eng. (1963) 525–527.
[30] M.Z. Kipp, G.C. Sih, The strain energy density failure criterion applied to notch elastic solids, Int. J. Solids Struct. 11 (1975) 153–173.
[31] H. Noguchi, Y. Furuya, A method of seamlessly combining a crack tip molecular dynamics enclave with a linear elastic outer domain in simulating elastic–plastic crack advance, Int. J. Fract. 87 (1997) 309–329.
[32] Y. Furuya, H. Nagachi, A combined method of molecular dynamics with micromechanics improved by moving the molecular dynamics region successively in the simulation of elastic–plastic crack propagation, Int. J. Fract. 94 (1998) 17–31.
[33] G.C. Sih, B. Liu, Meso-frature mechanics: a necessary link, in: G.C. Sih, V.E. Panin (Eds.), Prospects of Mesomechanics in the 21st Century, J. Theor. Appl. Fract. Mech. 37 (2002) 371–395.
[34] M.F. Horstemeyer, M.I. Baskes, Atomistic finite deformation simulations: a discussion on length scale effects in relation to mechanical stresses, J. Eng. Mater. Technol. 121 (1999) 114–119.
[35] M.F. Horstemeyer, M.I. Baskes, S. Plimpton, Computational nanoscale plasticity simulation using embedded atom potential, in: G.C. Sih, V.E. Panin (Eds.), Prospects of Mesomechanics in the 21st Century, J. Theor. Appl. Fract. Mech. 37 (2002) 49–98.
[36] P.A. Klein, J.W. Foulk, E.P. Chen, S.A.Wimmer, H.J. Gao, Physical model of brittle fracture: cohesive formulation and meshfree method, in: G.C. Sih, V.E. Panin (Eds.), Prospects of Mesomechanics in the 21st Century, J. Theor. Appl. Fract. Mech. 37 (2002) 99–166.
[37] W.G. Hoover, N.E. Hoover, W.C. Moss, Steady-state dislocation-motion via molecular dynamics, Phys. Rev. Lett. A 63 (1977) 321–326.
[38] F.F. Abraham, D. Bradbeck, R.A. Rafey, W.E. Rudge, Instability dynamics of fracture: a computer simulation investigation, Phys. Rev. Lett. 73 (1994) 272–275.